Assessing the Spectral Sensitivity of Martian Terrains to Iron Oxide Variations Using the SPLITS Model

Gladimir V. G. Baranoski, *Senior Member, IEEE*, Bradley W. Kimmel, T. Francis Chen, and Erik Miranda

***Abstract*—The mineralogy and environmental history of Mars are being extensively studied through remote sensing observations paired with laboratory and *in situ* experiments. A significant portion of these experiments is being devoted to the identification and mapping of different iron oxides present in the Martian terrains. Among these compounds, goethite has been an object of great interest since its occurrence can be interpreted as mineralogical evidence of past aqueous activity on those landscapes. Although such experiments can provide valuable information regarding the presence of these minerals, the scope of the resulting observations may be hindered by logistics and cost-related constraints. We believe that predictive computer simulations can be employed to mitigate some of these constraints and contribute to the generation and validation of hypotheses in this area. Accordingly, we propose the use of SPLITS (*Sp*ectral *Li*ght *T*ransport Model for *S*and) in investigations involving the spectral signatures of iron-bearing regions of Mars. In this paper, we initially demonstrate the predictive capabilities of the SPLITS model in this context through qualitative comparisons of modeled results with actual observations and measured data. Using the resulting modeled reflectance curves as our baseline data, we then perform a series of controlled computational experiments to investigate how variations on goethite and hematite content affect the spectral responses of Martian sand-textured soils.**

***Index Terms*—Iron oxide, Mars, reflectance, regolith, sand, simulation, spectral model.**

I. Introduction

MARS is covered by loose, particulate material, called regolith, characterized by the presence of iron oxides [1]–[3], such as hematite and goethite, whose spectral properties are directly associated with the overall reddish appearance of the Martian surface and the butterscotch color of the Martian sky (Fig. 1). The identification and mapping of these iron-rich compounds is central in geoscientific studies of the "red planet"– [4]. These minerals are indicators of environmental factors that are of relevance not only for the understanding of the origins of Martian terrains [5]–[7], but also for the search for potential environments that can sustain life on Mars [1], [8]. More specifically, iron oxides contain in their formula the ferrous (Fe^{2+}) and/or the ferric (Fe^{3+}) oxidation states of iron, which are considered to be associated with unweathered and weathered components of the Martian surface, respectively [1], [7]. For example, the ferric iron-oxide goethite forms as a product of aqueous processes in natural environments, and it has the hydroxide anion (OH^-) as an essential part of its structure ($\approx 10\%$ H_2O by weight) [6], [9]. These characteristics of goethite have led its identification in certain Martian terrains to be interpreted as mineralogical evidence of past aqueous activity on those areas [6], [9].

Arguably, the ferrous and ferric oxidation states of iron are the most spectrally active cations in the visible to near-infrared (VNIR) remote sensing of planetary surfaces [1], [7]. Accordingly, valuable scientific information about the mineralogy [6], [9], lithology [10], environmental history [1], [6] and astrobiology [8] of Martian regions covered by iron-rich regolith can be obtained through remote sensing observations coupled with measurements and simulations. Moreover, such combined efforts are crucial for the optimization of *in situ* investigations to be carried out by future missions to Mars [3], [5]. We note that remote observations paired with deterministic computer simulations are already providing relevant contributions to the analysis of Martian terrains with distinct morphological and mineralogical characteristics (e.g., [11] and [12]).

Laboratory experiments used in the investigation of Martian terrains usually employ soil analogs, or simulants [2], [13]–[18], since true Martian regolith samples are either not available [19] or might be too valuable [20] to be modified and contaminated by experimental procedures [3]. However, although soil analogs have been extensively used in studies regarding the thermal, mechanical, morphological, and chemical properties of Martian regolith, they have a limited applicability in investigations involving its spectral properties. This limitation is mostly due to the fact that certain mineralogical and physical properties (e.g., distinct iron oxide contents, density of parent material, and grain shape) cannot be effectively mimicked or controlled in experiments involving regolith simulants [3].

In order to overcome the investigation constraints mentioned above, we propose the use of a simulation framework that allows for systematic computational experiments involving the spectral properties of sandy landscapes and regolith-covered terrains found in Mars. Within this framework, the light interactions with the particulate materials forming these regions are simulated using a stochastic computer model, known as SPLITS (*Sp*ectral *Li*ght *T*ransport Model for *S*and) [21], that accounts for the morphological and mineralogical characteristics of the constituent grains of these materials and their distribution in the pore medium [22]. Employing the proposed framework, researchers can change selected material parameters and analyse their effects on the spectral signature

Manuscript received October 01, 2014; revised November 27, 2014; accepted January 26, 2015. Date of publication February 25, 2015; date of current version August 11, 2015. This work was support in part by the Natural Sciences and Research Council of Canada (NSERC) under Grant 238337.

The authors are with the Natural Phenomena Simulation Group (NPSG), David R. Cheriton School of Computer Science, University of Waterloo, Waterloo, ON N2L 3G1, Canada (e-mail: gvgbaran@cs.uwaterloo.ca).

Color versions of one or more of the figures in this paper are available online at http://ieeexplore.ieee.org.

Digital Object Identifier 10.1109/JSTARS.2015.2400228

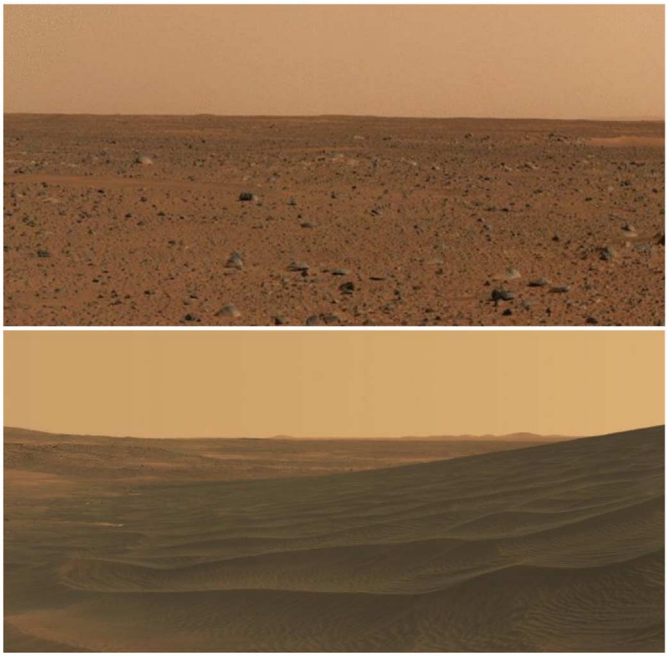

Fig. 1. Photos of the Gusev crater taken by the panoramic camera on board the Mars Exploration Rover Spirit (courtesy of NASA).

of these regions while keeping the other parameters constant. In fact, SPLITS can be run online [23] via a model distribution system [24] that enables researchers to specify experimental conditions (e.g., angle of incidence and spectral range) and material parameters (e.g., amount of iron oxides, soil texture and particle type distribution), and receive customized simulation results.

In this paper, which is an extended and updated version of a conference presentation [25], we initially describe a first round of computational experiments performed to demonstrate the predictive capabilities of the SPLITS model with respect to the qualitative reproduction of spectral trends associated with Martian regolith. In these experiments, we qualitatively compared modeled results with actual observations and measured data available for five iron-bearing regions of Mars, namely the Olympus-Amazonis [26], the Oxia Palus [26], and three different sites located in the Gusev crater [27]. We then present a second round of computational experiments performed to qualitatively assess the impact of goethite and hematite on the spectral signatures of Martian iron-rich regolith. In these experiments, we employed as baseline the modeled results obtained in the first round.

Although the presence of iron oxides is known to significantly affect the spectral signatures of sandy landscapes [7], [14], to the best of our knowledge, controlled computational experiments to qualitatively investigate the sensitivity of these signatures with respect to specific changes on goethite and hematite content have not been performed to date with respect to Martian sand-textured soils. From a scientific point of view, such an investigation could contribute to enhance the procedures for the identification and mapping of these minerals through remotely deployed devices. We remark that such controlled experiments, in which only specific sample parameters associated with the presence of selected minerals (e.g., ratio of hematite to goethite and their respective mass fractions) are varied while all other material parameters are kept fixed, have limited feasibility under actual laboratory conditions due to the practical issues mentioned earlier. For example, these experiments would require the removal or replacement of one mineral by another (e.g., goethite by hematite) while keeping the same ratio of pure, mixed, and coated particles. Clearly, these are not low-cost processes to be performed in true samples, which are not readily available in the first place [19], [20].

This paper is organized as follows. In Section II, we briefly outline the material characterization data, the reference datasets, and the computational procedures employed in this work. In Section III, we report our findings and discuss their theoretical and practical implications. Finally, in Section IV, we close this paper and outline directions for future research in this area.

II. Materials and Methods

A. Particulate Material Characterization Data

We employed physical data obtained for Martian regolith whenever such data was available (e.g., porosity of 60% [28]), and average data associated with terrestrial sandy soils otherwise. For example, it has been stated that the regolith materials found in the reference regions considered in this work, namely the Olympus-Amazonis [26], the Oxia Palus [26], and three different sites located in the Gusev crater [27], contain iron oxides such as hematite, goethite, and magnetite, and have basalt as their primary parent material [6], [9], [27], [29]. Accordingly, in our simulations, we employed basalt (with a density of 3 kg/L [29]) as the parent material, and considered the iron oxides appearing as pure particles [1], contaminants in the parent material [30], or coatings within an illite matrix [31]. The particle-type distributions considered in the simulations are thus given in terms of the percentages of pure (μ_p), mixed (μ_m), and coated (μ_g) grains [21], [32].

We remark that the SPLITS model takes into account the individual morphological characteristics of the material constituent grains. More specifically, their sphericity and roundness are normally distributed, with their mean and the standard deviation derived from data provided by Vepraskas and Cassel [33], and constrained to fall within their respective ranges derived from the same data (Table I). Their size, represented by their diameter D is distributed according to a piecewise log-normal distribution as suggested by Shirazi *et al.* [34], i.e., $\log D$ is normally distributed. This distribution is characterized by two parameters, namely the geometric mean particle diameter d_i and its standard deviation σ_i, which are functions of the soil texture. That is, the percentages of the sand-sized, silt-sized, and clay-sized particles are employed to compute the respective geometric mean diameters and standard deviations of these particles using a particle-size distribution provided by Shirazi *et al.* [34]. In this work, the values provided for these parameters are listed in Table II. Note that the presence of clay-sized particles was assumed to be negligible. The reader interested in

TABLE I
MEAN, STANDARD DEVIATION, AND RANGE VALUES FOR SPHERICITY AND ROUNDNESS PROVIDED BY VEPRASKAS AND CASSEL [33]

	Mean	Standard deviation	Min.	Max.
Roundness	0.482	0.072	0.2	0.7
Sphericity	0.798	0.064	0.6	0.95

TABLE II
GEOMETRIC MEAN PARTICLE DIAMETERS (GIVEN IN MM) AND STANDARD DEVIATIONS FOR DIFFERENT MIXTURES OF SAND-SIZED PARTICLES (s_1) AND SILT-SIZED PARTICLES (s_2)

Percentages		Sand		Silt	
s_1	s_2	d_1	σ_1	d_2	σ_2
85	15	0.112	2.170	0.173	3.320
95	5	0.155	1.990	0.640	4.720

The diameters and standard deviations for sand-sized particles (d_1 and σ_1, respectively) and silt-sized particles (d_2 and σ_2, respectively) are provided by Shirazi *et al.* [34].

TABLE III
INPUT DATASETS I, II, III, IV, AND V USED TO OBTAIN MODELED REFLECTANCE CURVES FOR FIVE SITES ON DISTINCT REGIONS OF MARS: OLYMPUS-AMAZONIS, OXIA PALUS, AND GUSEV CRATER (SITES D-GREEN, D-RED, AND E-GREEN), RESPECTIVELY

Dataset	s_1	s_2	μ_p	μ_m	μ_c	r_{hg}	ϑ_{hg}	ϑ_m
I	85	15	0	90	10	0.75	0.005	0.00
II	95	5	0	100	0	0.15	0.070	0.00
III	85	15	0	100	0	0.25	0.030	0.00
IV	95	5	0	100	0	0.20	0.030	0.00
V	85	15	10	80	10	0.50	0.030	0.01

The texture of the samples is described by the percentages (%) of sand and silt (represented by s_1 and s_2, respectively). The particle-type distributions considered in the simulations are given in terms of the percentages of pure (μ_p), mixed (μ_m), and coated (μ_g) grains. The parameter r_{hg} corresponds to the ratio between the mass fraction of hematite to the total mass fraction of hematite and goethite, which is given by ϑ_{hg}. The parameter ϑ_m represents the mass fraction of magnetite.

more details about the parameter space of the SPLITS model is referred to related publications [21], [32].

The remaining parameter values used to obtain the modeled reflectance curves associated with the five reference Martian regions are given in Table III. These include the ratio between the mass fraction of hematite to the total mass fraction of hematite and goethite, denoted by r_{hg}, the total mass fraction of hematite and goethite, denoted by ϑ_{hg}, and the total mass fraction of magnetite, denoted by ϑ_m. For example, in the case of dataset I, the percentage of hematite and goethite corresponds to 0.5% ($\vartheta_{hg} = 0.005$), with hematite contributing to 75% of the total amount of hematite and goethite ($r_{hg} = 0.75$), and the percentage of magnetite corresponds to 0% ($\vartheta_m = 0$).

The refractive indices and extinction coefficients for the iron oxides considered in our simulations, namely hematite, goethite, and magnetite, are depicted in Fig. 2. The data for goethite was originally referred by Egan and Hilgeman [35] as limonite data. We note, however, that limonite is the general term for hydrous ferric iron oxides, and it is mostly employed to denote goethite [36]. The refractive indices for the coating and parent materials considered in our simulations, namely illite and basalt, respectively, are depicted in Fig. 3.

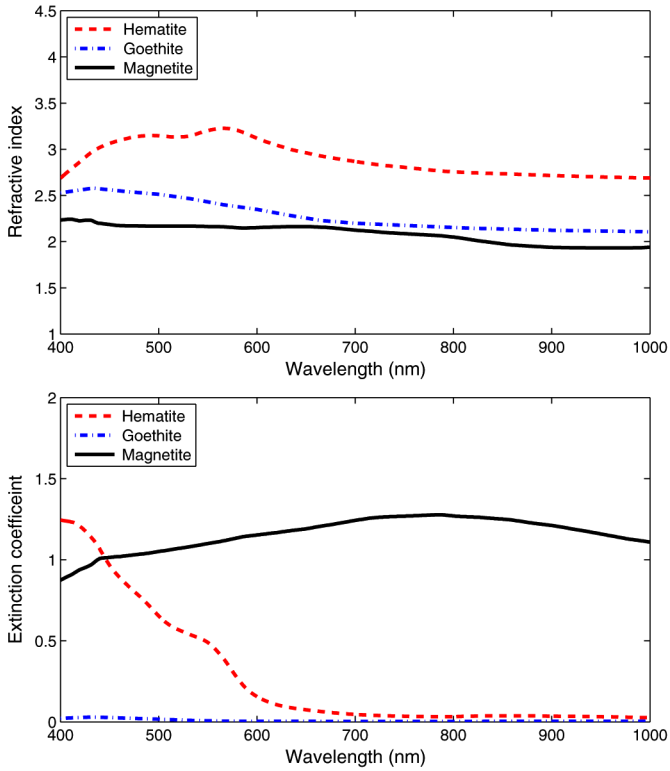

Fig. 2. Spectral data for the iron oxides accounted for in our simulations: hematite [37], goethite [35], and magnetite [38]. Top: refractive index (real part). Bottom: extinction coefficient (refractive index, imaginary part).

B. Spectral Reference and Modeled Datasets

The main purpose of the comparisons depicted in this paper is to assess the use of computer simulations in qualitative investigations involving the spectral properties of Martian sand-textured soils. Since an exhaustive comparison with all spectral datasets available in the literature is beyond the scope of this work, we selected as reference the spectral datasets provided by Mustard and Bell [26], depicted in several relevant works in this area (e.g., [3], [7], [10], [15], [39]), and spectral datasets obtained more recently by Bell *et al.* [27] through *in situ* measurements. Despite limitations associated with the actual observation and measurement conditions (e.g., coarse spatial resolution [26] and possible small variations due to topographic effects [27]), these spectral datasets capture the main qualitative spectral trends observed in the target Martian sand-textured soils, and are consistent with related observations reported in the literature (e.g., [7], [8]).

The measured spectra for the Olympus-Amazonis and the Oxia Palus regions provided by Mustard and Bell [26] (Fig. 4) were obtained by merging data acquired through the ISM (Imaging Spectrometer for Mars) experiment on the 1989 Soviet Phobos-2 mission with Earth-based telescopic observations of Mars. More precisely, ISM data in 750–1510 nm region, which was acquired with a spectral resolution of 22.5 nm and a spatial resolution of 22×22 km [40], was combined with Earth-based telescopic observations in the 400–1000 nm region, which were acquired with a spectral resolution of 9 nm and a spatial resolution of 500–600 km with respect

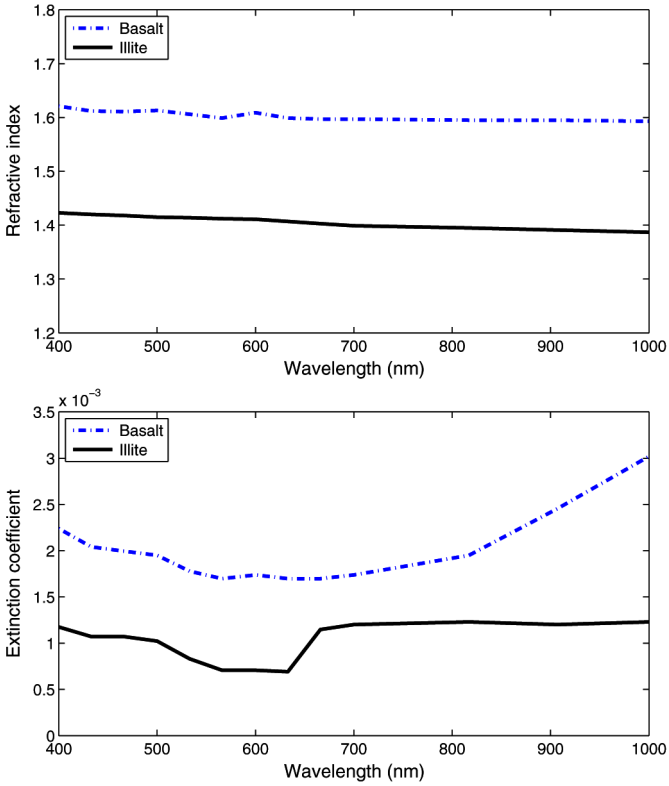

Fig. 3. Spectral data for the coating matrix and parent material considered in our simulations, namely illite [35] and basalt [35], respectively. Top: refractive index (real part). Bottom: extinction coefficient (refractive index, imaginary part).

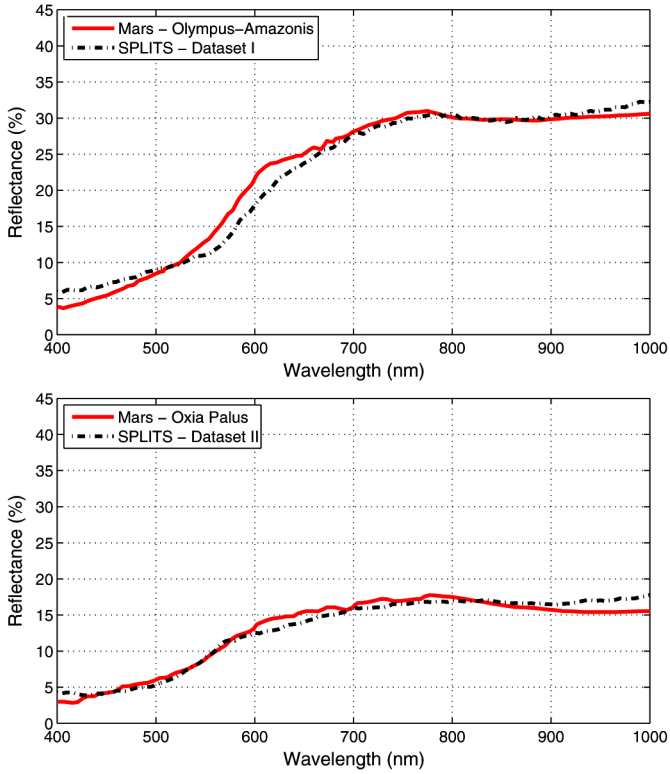

Fig. 4. Qualitative comparisons of measured and modeled spectra for bright (Olympus-Amazonis) and dark (Oxia Palus) regions of Mars. The measured composite spectra provided by Mustard and Bell [26] was obtained by merging data acquired through the ISM experiment on the 1989 Soviet Phobos-2 mission with Earth-based telescopic observations of Mars, and removing atmospheric absorptions. Top: Olympus-Amazonis region. Bottom: Oxia Palus region. The modeled data were obtained employing the SPLITS model [21], [23] and using the input datasets I and II, respectively, given in Table III.

to diameter of the observation spots [41]. The telescopic data was scaled to the ISM data in the 770–930 nm region [26]. According to Mustard *et al.* [26], [40], atmospheric absorptions were removed from the ISM data. In the case of the telescopic data, according to Bell *et al.* [41], most or all of the debilitating effects of the terrestrial atmosphere were removed and there was little dust storm activity on Mars during the times of observation resulting in a Martian atmosphere free of optically thick airborne dust.

Within the SPLITS algorithmic ray optics formulation, a ray interacting with a given material sample can be associated with any selected wavelength within the 400–1000 nm region of interest [21]. Hence, SPLITS can provide reflectance readings with different spectral resolutions. For consistency, however, we considered a spectral resolution of 5 nm in all modeled curves depicted in this work. In terms of illumination and collection geometries, the SPLITS model can provide bidirectional reflectance quantities [21] by recording the direction of the outgoing rays using a virtual gonioreflectometer [42]. In addition, one can obtain directional-hemispherical reflectance quantities [43] by integrating the outgoing rays with respect to the collection hemisphere using a virtual spectrophotometer [44], [45]. Similarly, bihemispherical or biconical quantities can be calculated by integrating bidirectional reflectance values with respect to the incident and collection hemispheres [21], [42].

The fact that the composite datasets provided by Mustard *et al.* [26] cover very large areas makes their comparison with bidirectional simulation readings inappropriate. Hence, we selected to compare them with directional-hemispherical readings (Fig. 4) for consistency with the literature. For example, these composite datasets have been qualitatively compared with directional-hemispherical reflectance readings obtained for the Mars soil simulant JSC Mars-1 by Allen *et al.* [13], [15], [16] and Sieferlin *et al.* [3] (Fig. 5). Recently, Maturilli *et al.* [17] and Pommerol *et al.* [18] obtained biconical reflectance and bidirectional reflectance readings, respectively, for the the same soil simulant. The qualitative trends were exactly the same as the directional-hemispherical readings obtained by Allen *et al.* [13], [15], with the quantitative differences being unremarkable. We also note that Allen *et al.* [15] mentioned that their reflectance readings closely agree with the spectrum obtained by Morris *et al.* [46] for another soil simulant, which was obtained using a Cary-14 directional-hemispherical spectrometer. The same device was used to obtain the directional-hemispherical reflectance measurements used by Bell *et al.* [47] in the calibration of the reflectance datasets measured at the Gusev crater sites, which are also employed as qualitative references in this work (Fig. 6).

The modeled directional-hemispherical reflectance curves computed by SPLITS were obtained casting 10^6 rays from an angle of incidence equal to 0°, and collecting all rays reflected

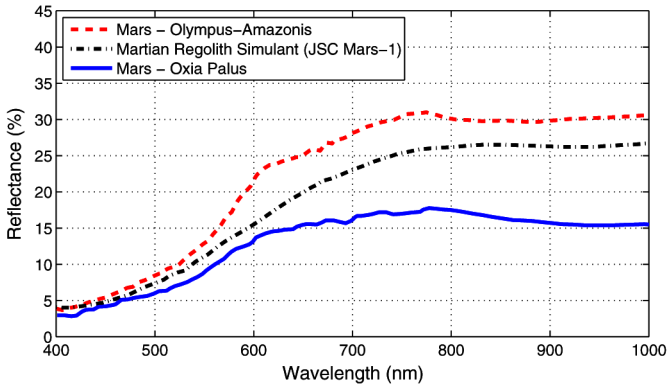

Fig. 5. Qualitative comparisons of measured spectra for bright (Olympus-Amazonis) and dark (Oxia Palus) regions of Mars provided by Mustard and Bell [26] with the measured spectrum of a Martian regolith simulant (JSC Mars-1) provided by Allen *et al.* [13], [15], [16].

into the upper hemisphere using a virtual spectrophotometer [44]. Recall that reflectance is defined as the ratio of reflected to incident flux [48], while reflectance (radiance) factor is defined as the ratio of the radiant flux actually reflected by a sample surface to that which would be reflected into the same reflected-beam geometry by a diffuse standard surface irradiated in the exactly same way [49], [50]. According to Judd [49] and Nicodemus [50], the directional-hemispherical reflectance and the hemispherical-directional reflectance (radiance) factor are numerically equivalent for a given direction as a direct consequence of the Kirchhoff's law [51] and the Helmholtz reciprocity principle [49]. The reader interested in the mathematical derivation of this numerical equivalence is referred to the seminal papers by Judd [49] and Nicodemus [51]. Hence, in practical applications involving reflectance measurements for materials characterized by a predominant diffuse behavior, these quantities are often used interchangeably [52]. For example, the spectra associated with the three sites at the Gusev crater, also employed as reference in this work (Fig. 6), were obtained using a multispectral (11 channels) imaging system (panoramic camera, also referred to as Pancam camera) on board the Mars Exploration Rover Spirit, and described in terms of reflectance (radiance) factor by Bell *et al.* [27]. In the paper addressing the calibration of the device used in their acquisition, these quantities are described by Bell *et al.* [47] in terms of directional-hemispherical reflectance.

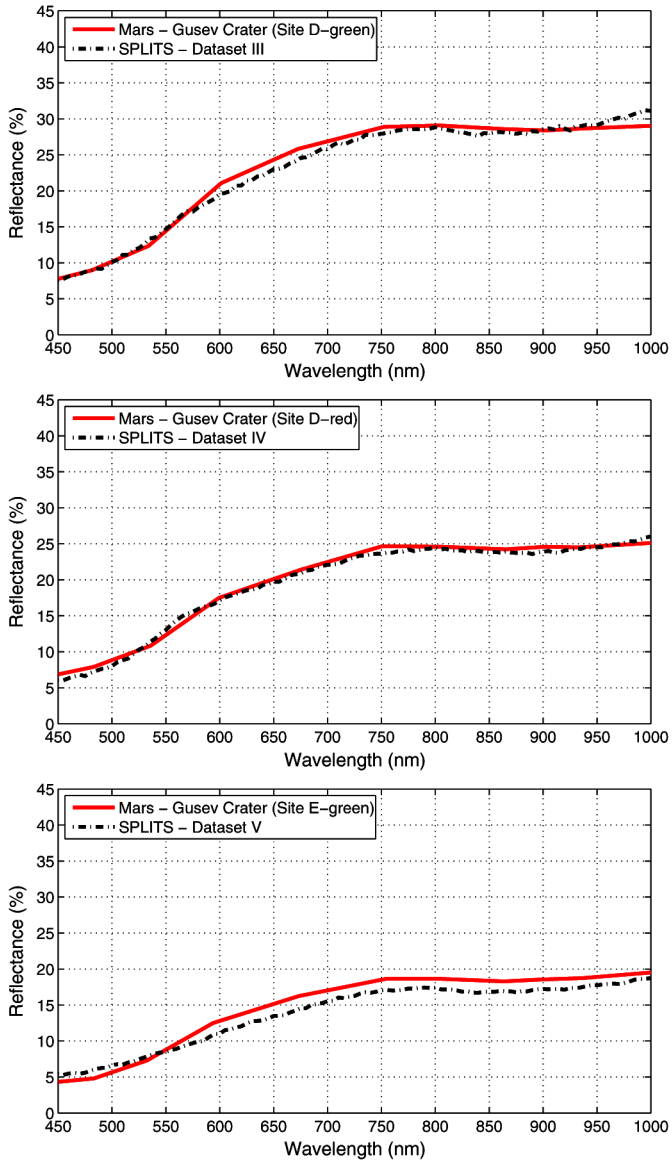

Fig. 6. Qualitative comparisons of measured and modeled spectra for different sites at the Gusev crater on Mars. The measured spectra provided by Bell *et al.* [27] was obtained from multispectral images acquired using a digital imaging system (panoramic camera) on board the Mars Exploration Rover Spirit. Top: site D-green. Middle: site D-red. Bottom: site E-green. The modeled data was obtained employing the SPLITS model [21], [23] and using the input datasets III, IV, and V, respectively, given in Table III. Note that we consider a lower limit of 450 nm for consistency with the actual measured data.

C. Computational Experiments

Our computational experiments are divided into two rounds. In the first round, we assessed the predictive capabilities of the SPLITS model and obtained modeled reflectance curves for the five reference Martian regions using the datasets provided in Table III. In the second round of experiments, we assessed the impact of variations on the hematite and goethite contents. Since different contents of hematite and goethite have been assigned to the five datasets (Table III) used to obtain modeled reflectance curves, in order to strengthen our assessment of the impact of each of these minerals, we consider test cases that allowed us to examine the effects resulting from the complete removal of one them, namely goethite, whose identification has been connected to the putative aqueous activity in early Martian environments [6], [9]. Note that by removing goethite, we were also able to assess the individual impact of hematite, arguably the most investigated iron oxide in connection with geoscientific studies about Mars [1], [4], [5], [9], [10].

To compose these test cases, we computed the corresponding reflectance curves using modified versions of the baseline datasets used to compute the modeled curves during the first round of experiments. In these modified versions of the datasets, only specific parameters were changed (one at a time):

the ratio between the mass fraction of hematite to the total mass fraction of hematite and goethite (r_{hg}), and the total mass fraction of hematite and goethite (ϑ_{hg}).

After the two rounds of experiments outlined above, we performed a parameter differential sensitivity analysis [53], [54], also known as direct sensitivity analysis. It consists in the computation of a sensitivity index for a specific parameter. This index, which was introduced by Hoffman and Gardner [55] to evaluate uncertainties in environmental assessment models, provides the ratio of the change in output to the change in the selected parameter while all other parameters remain fixed. A sensitivity index of 1.0 indicates complete sensitivity (or maximum impact), while a sensitivity index less than 0.01 indicates that the output is insensitive to changes in the parameter [55]. Accordingly, we computed the mean sensitivity index (MSI) for the spectral regions of interest to assess the mean ratio of change in reflectance to the change in the specific parameters (r_{hg} and ϑ_{hg}, one at the time) associated with the iron oxide contents. This index is expressed as

$$MSI = \frac{1}{N}\sum_{i=1}^{N}\frac{|\rho_b(\lambda_i) - \rho_m(\lambda_i)|}{\max\{\rho_b(\lambda_i), \rho_m(\lambda_i)\}} \quad (1)$$

where ρ_b and ρ_m correspond to the reflectances associated with the baseline and modified datasets, respectively, and N is the total number of wavelengths sampled with a 5-nm resolution within a selected spectral region.

We remark that the purpose of our sensitivity investigations is twofold, namely to assess the influence (impact) of key parameters (in our case associated with iron oxide contents) and to guide future research efforts in this area. Accordingly, in order to assess this influence, we employed the sensitivity index, arguably one of the most reliable sensitivity measures [54]. We note that other sensitivity measures are available in the literature, and the readers interested in an extensive comparison of their performance and reliability are referred to the comprehensive reviews by Hamby [53], [54]. In addition, readers interested in issues directly related to model inversion procedures or associated with the extraction of information from hyperspectral images, which are outside the scope of this work, are referred to related works in these areas [56]–[59].

III. Results and Discussion

Initially, we qualitatively compared modeled results with measured spectra for the Olympus-Amazonis and Oxia Palus regions [26]. We remark that the measured curves depicted in Fig. 4 correspond to composite spectra obtained for large areas by merging data captured using a scanning imaging spectrometer from the altitude of orbit of 6300 km [40] with data acquired using Earth-based telescopic observations [41] (Section II-B). As a result, these measured composite spectra incorporate a certain degree of spatial and temporal variabilities that cannot be fully reproduced through simulations, either based on computer models (Fig. 4) or regolith simulants (Fig. 5), associated with discrete experimental conditions. Despite these constraints, the modeled reflectance curves obtained using SPLITS captured the main qualitative trends depicted in the measured reflectance curves, as it can be observed in the graphs presented in Fig. 4. For example, it has been widely observed that most Martian surface materials bearing ferric oxides, such as hematite and goethite, are characterized by a smooth reflectance increase toward the red-end of the visible light spectrum, with a slope varying from region to region on Mars and a peak between 700 and 800 nm [7], [8]. These spectral features are reproduced in the modeled reflectance curves depicted in Fig. 4.

In order to further examine the predictive capabilities of the SPLITS model, we also compared modeled reflectance spectra with *in situ* measured spectra for different sites at the Gusev crater. These measured spectra were acquired through a multispectral imaging system on board the Mars Exploration Rover Spirit, and they were estimated to be within a 5%–10% absolute accuracy [27]. The system was mounted on a mast assembly ≈ 1.5 m above the Martian surface, rendering any atmospheric influence negligible. It is worth noting, however, that the measured spectra was not corrected for local topographic effects [27]. Although this aspect makes direct quantitative comparisons difficult, it does not preclude qualitative comparisons. As it can observed in the graphs presented in Fig. 6, the modeled curves show good qualitative agreement with their measured counterparts. We note that this level of qualitative agreement was achieved despite the fact that not all minerals found in these regions could be accounted for in the simulations due to the lack of reliable supporting data such as spectral indices of refraction and extinction coefficients.

In our next round of computational experiments, we compared modeled spectra (Figs. 7 and 8) obtained using modified versions of the baseline datasets I–V (Table III) associated with two test cases outlined in Section II-C. In test case 1, we replaced goethite by hematite (resulting in $r_{hg} = 1$) without changing to total mass fraction of the iron oxides, i.e., keeping (ϑ_{hg}) fixed (baseline value). In test case 2, we reduced the total iron oxide content by setting ϑ_{hg} equal to original (baseline) mass fraction of hematite, while maintaining $r_{hg} = 1$. We also compute MSI values (Figs. 9 and 10) to further assess the impact of the goethite and hematite content changes (associated with the two test cases) across the visible (400–700 nm), NIR (700–1000 nm) and VNIR (400–1000 nm) regions of interest.

As it can be observed in the graphs associated with datasets I and II presented in Fig. 7, the replacement of goethite by hematite (case 1) resulted in a decrease in reflectance values within the 400–1000 nm range, which was expected considering the stronger absorptive behavior of hematite in comparison with the absorptive behavior of goethite (Fig. 2). For dataset II, which had the smallest and largest mass fractions initially assigned to hematite and goethite, respectively, this replacement resulted in a more pronounced reflectance decrease. This can be explained by the fact that the replacement of goethite by hematite resulted in a more substantial increase in the hematite content. Note that in the region below 500 nm, the extinction coefficient of hematite is characterized by high values (Fig. 2). Consequently, an increase in the hematite content did not lead to a significant decrease in reflectance in this region since absorption was already high below 500 nm due to the corresponding high extinction coefficient values of this mineral. This behavior is also reflected in the MSI values computed for dataset II

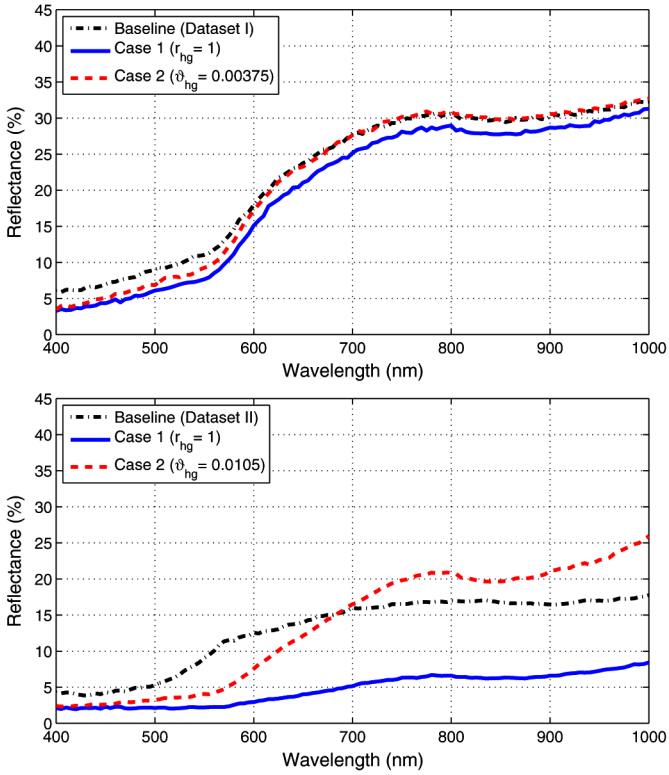

Fig. 7. Comparison of modeled spectra obtained considering two test cases using as baseline the datasets I (top) and II (bottom) provided in Table III. Case 1: replacement of the goethite by hematite (resulting in $r_{hg} = 1$) without changing to total mass fraction of the iron oxides, i.e., keeping (ϑ_{hg}) fixed (baseline value). Case 2: reduction of total iron oxide content by setting ϑ_{hg} equal to original (baseline) mass fraction of hematite, while maintaining $r_{hg} = 1$.

(Fig. 9), which indicated a slightly stronger impact in the NIR region in comparison with the visible region.

With respect to test case 2, the reduction of the total iron content (now formed only by hematite) to the initial hematite content resulted in distinct behaviors as indicated by the corresponding curves presented in Fig. 7. More specifically, one can observe a significant reflectance increase in NIR region for the modified dataset II with respect to the associated baseline curve. We remark that this dataset had the smallest and largest mass fractions initially assigned to hematite and goethite, respectively. It is worth mentioning that the replacement of goethite by hematite followed by the total iron oxide content reduction is equivalent to substituting the particles of goethite in the mixed grains by hematite, effectively resulting in the removal of goethite, while keeping the same original (baseline) content of hematite.

Hence, comparing case 2 (hematite only) for dataset II (Fig. 7) with the corresponding baseline case (with hematite and goethite), the reflectance decrease in the visible region can be explained by the high extinction coefficient values of hematite below 700 nm (Fig. 2). In contrast, the reflectance increase in the NIR region can be attributed to the high refractive index values of hematite in this region since both hematite and goethite are characterized by low extinction coefficient values above 700 nm (Fig. 2).

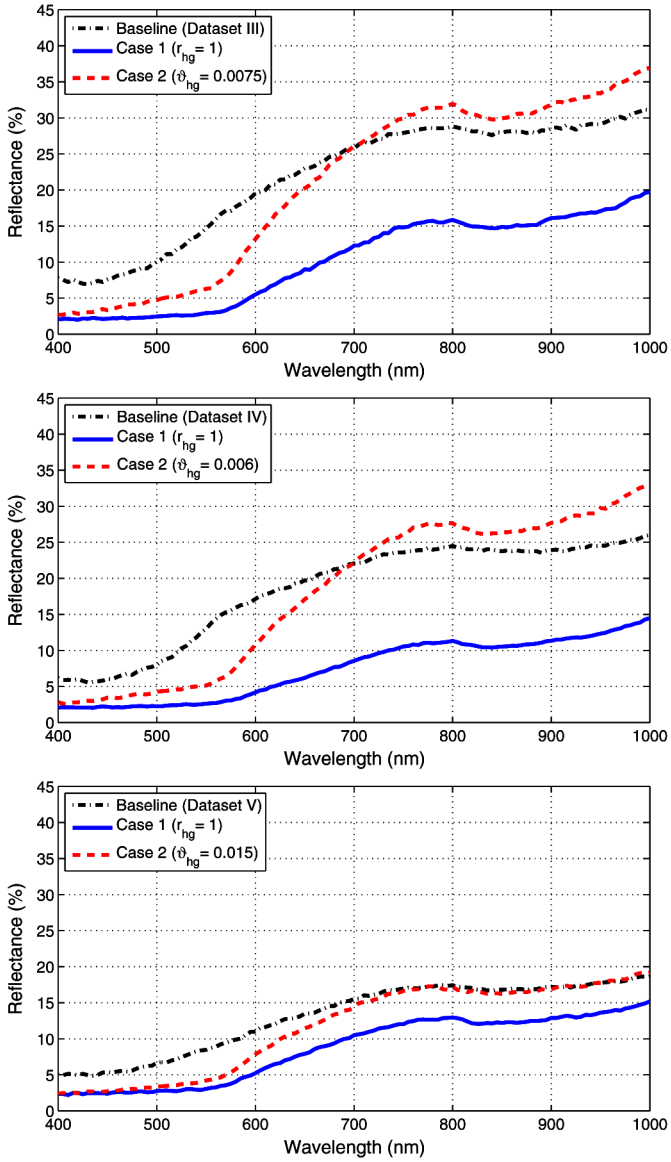

Fig. 8. Comparison of modeled spectra obtained considering two test cases using as baseline the datasets III (top), IV (middle), and V (bottom) provided in Table III. Case 1: replacement of the goethite by hematite (resulting in $r_{hg} = 1$) without changing to total mass fraction of the iron oxides, i.e., keeping (ϑ_{hg}) fixed (baseline value). Case 2: reduction of total iron oxide content by setting ϑ_{hg} equal to original (baseline) mass fraction of hematite, while maintaining $r_{hg} = 1$.

Comparing the baseline curves for both datasets with their respective case 2 (hematite only) curves, one can also observe a less pronounced reflectance slope in the 600–800 nm range (Fig. 7) for dataset II, which can be attributed to the more dominant presence of goethite associated with this dataset. This spectral smoothing role of goethite can be explained by the fact that the extinction coefficient values of goethite are more uniform in comparison with the extinction coefficient values of hematite across the 600–800 nm range (Fig. 2).

When we repeated the simulations considering modified versions of datasets III, IV, and V (Fig. 8), we detected the same trends reported for datasets I and II. For example, regarding

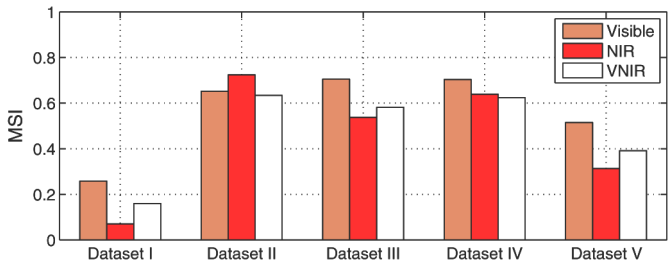

Fig. 9. Comparison of MSI values illustrating the impact of replacing goethite content by hematite without changing to total mass fraction of the iron oxides (case 1). The MSI values were computed for each modified reflectance curve (across selected visible (400–700 nm), NIR (700–1000 nm), and VNIR (400–1000 nm) ranges), and considering the respective baseline curve associated with a given dataset (Table III).

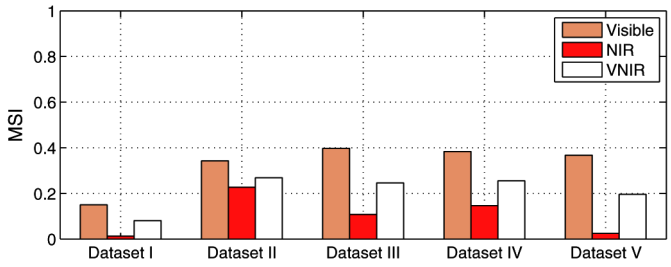

Fig. 10. Comparison of MSI values illustrating the impact of reducing the total iron oxide content, without goethite, to the original (baseline) mass fraction of hematite (case 2). The MSI values were computed for each modified reflectance curve (across selected visible (400–700 nm), NIR (700–1000 nm), and VNIR (400–1000 nm) ranges), and considering the respective baseline curve associated with a given dataset (Table III).

datasets III and IV, which, like dataset II, had dominant mass fractions initially assigned to goethite in the baseline case, one can also observe a reflectance decrease in the visible region, and an increase in NIR region when comparing the curves obtained for case 2 with the curves obtained for the baseline case. Moreover, these simulations considering datasets III and IV further illustrate the spectral smoothing role of goethite in the 600–800 nm region, which becomes more evident when one compares the baseline case (with goethite and hematite) with case 2 (without goethite, but with the same iron content depicted in the baseline case).

The MSI values computed for case 1 (Fig. 9) indicate that the impact of replacing goethite by hematite, without changing the total mass fraction of these minerals (case 1), was substantially larger for datasets II, III, and IV, in which lower initial mass fractions were initially assigned to hematite (Table III). In contrast, the lowest impact was observed for the curve obtained using a modified version of dataset I, which had the largest initial mass fraction initially assigned to hematite in the baseline case.

The MSI values computed for case 2 (Fig. 10) indicate that the reduction of the total iron content to the initial hematite content resulted in a lower overall impact in comparison with the MSI values for case 1 depicted in Fig. 9. Due to the dominant role of hematite as the strongest absorber considered in our simulations (Figs. 2 and 3), a reduction of its content was expected to lead to a reduction of its overall impact. We remark that the replacement of goethite by hematite followed by the total iron oxide content reduction is equivalent to substituting the particles of goethite in the mixed grains by hematite. Accordingly, the smallest impact associated with the replacement of goethite by hematite was observed for the modified dataset I (Fig. 10) since it had the smallest and largest mass fractions initially assigned to goethite and hematite, respectively, in the baseline case (Table III). This, in turn, resulted in the smallest variation of hematite content among all five modified datasets and, consequently, in the smallest MSI values computed for the selected spectral ranges.

Although the spectral properties of particulate materials made up of minerals with different composition, size, and distribution can be associated with the distinct characteristics of the spectral indices of its main absorbers, such as hematite and goethite in the case of Martian iron-rich regolith, they should not necessarily be expected to precisely match laboratory references for these absorbers in pure form [7]. Viewed in this context, our investigation demonstrates that predictive computer simulations capable of accounting for complex phenomena through first principles modeling approaches can be instrumental in the pursuit of a better understanding about the spectral properties of these materials. The observations derived from our computer experiments are consistent with observations reported in the literature about the strong influence of hematite [1], [7] and the smoothing role of goethite [7], [9] in the spectral signature of Martian iron-bearing terrains. Hence, we are confident that the proposed simulation framework can be effectively employed to assist future investigations involving the spectral properties of Martian sand-textured terrains.

IV. Conclusion and Future Work

We believe that the integration of remote sensing data with predictive modeling will continue to play an important role in investigations involving the spectral properties, mineralogy, lithology, and environmental history of Martian landscapes. The simulations reported in this work show that the proposed simulation framework based on the SPLITS model has the flexibility and predictive capabilities required to support such investigations.

As stated by Bell and Ansty [7], the main characteristics of early Martian landscapes may still be preserved in the present regolith covering the planet's surface. Accordingly, one of the key challenges for the advancement of research on Martian environmental history involves the establishment of diagnostic spectral procedures for the identification of distinct surface material constituents among several iron-bearing compounds mixed in unknown proportions [7]. Furthermore, the occurrence of these compounds is characterized by specific morphological attributes that cannot be properly reproduced and studied under traditional laboratory conditions. Hence, by providing reliable insights about spectral trends associated with the presence of iron oxides in Martian regolith, controlled computational experiments can contribute for the development of such procedures and, consequently, to the correct interpretation of geophysical

clues leading to a more comprehensive understanding of the origins of Martian landscapes.

As future work, we intend to employ the proposed framework in the study of different hypotheses related to weathering processes involved in the formation of Martian terrains, and in the investigation of the interplay between light scattering phenomena taking place at the ground and atmospheric levels. For the latter, we may resort, e.g., to support data derived from observations provided by the OMEGA (Observatoire pour la Minéralogie, l'Eau, les Glaces et l'Activité) imaging spectrometer on board Mars Express [11], [60], and multiangle observations acquired by the CRISM (Compact Reconnaissance Imaging Spectrometer for Mars) instrument on board the Mars Reconnaissance Orbiter [56], [57], [61]. We also intend to extend our research to other planetary bodies, such as Venus and Titan, as more supporting morphological and spectral data becomes available.

REFERENCES

[1] D. Catling and J. Moore, "The nature of coarse-grained crystalline hematite and its implications for the early environment of Mars," *Icarus*, vol. 165, pp. 277–300, 2003.

[2] K. Edgett and N. Lancaster, "Volcaniclastic aeolian dunes: Terrestrial examples and applications to Martian sands," *J. Arid Environ.*, vol. 25, pp. 271–297, 1993.

[3] K. Seiferlin *et al.*, "Simulating Martian regolith in the laboratory," *Planet. Space Sci.*, vol. 56, pp. 2009–2025, 2008.

[4] P. R. Christensen, R. Morris, M. Lane, L. Bandfield, and M. C. Malin, "Global mapping of Martian hematite mineral deposits: Remnants of water-driven processes on early Mars," *J. Geophys. Res.*, vol. 106, no. E10, pp. 23 873–23 885, 2000.

[5] P. R. Christensen *et al.*, "Detection of crystalline hematite mineralization on Mars by the Thermal Emission Spectrometer: Evidence for near-surface water," *J. Geophys. Res.*, vol. 105, no. E4, pp. 9623–9642, 2000.

[6] R. Morris *et al.*, "Mössbauer mineralogy of rock, soil, and dust at Gusev crater, Mars: Spirit's journey through weakly altered olivine basalt on the plains and pervasively altered basalt in the Columbia Hills," *J. Geophys. Res.*, vol. 11, no. E02S13, pp. 1–28, 2006.

[7] J. F. Bell III and T. M. Ansty, "High spectral resolution UV to near-IR observations of Mars using HST/STIS," *Icarus*, vol. 191, pp. 581–602, 2007.

[8] J. Bishop, M. Dyar, M. Lane, and J. Banfield, "Spectral identification of hydrated sulfates on Mars and comparison with acidic environments on Earth," *Int. J. Astrobiol.*, vol. 3, no. 4, pp. 275–285, 2004.

[9] R. Morris and D. Golden, "Goldenrod pigments and the occurrence of hematite and possibly goethite in the Olympus-Amazonis region of mars," *Icarus*, vol. 134, pp. 1–10, 1998.

[10] R. Morris, D. Golden, and J. F. Bell III, "Low-temperature reflectivity spectra of red hematite and the color of Mars," *J. Geophys. Res.*, vol. 102, no. E4, pp. 9125–9133, 1997.

[11] S. Douté *et al.*, "South pole of Mars: Nature and composition of icy terrains from Mars Express OMEGA observations," *Planet. Space Sci.*, vol. 55, pp. 113–133, 2007.

[12] F. Poulet *et al.*, "Quantitative compositional analysis of Martian mafic regions using the MEx/OMEGA reflectance data 2. Methodology, uncertainties and examples of application," *Icarus*, vol. 201, pp. 69–83, 2009.

[13] C. Allen, R. Morris, D. Lindstrom, M. Lindstrom, and J. Lockwood, "JSC MARS-1: Martian regolith simulant," in *Proc. Lunar Planet. Inst. Sci. Conf. Abstr.*, 1997 vol. 28, p. 1797.

[14] K. Kuhlman, J. Marshall, N. Evans, and A. Luttge, "Australian red dune sand: A potential Martian regolith analog," in *Proc. Workshop Martian Highlands Mojave Desert Analogs*, Barstow, CA, USA, 2001, pp. 4021–4022.

[15] C. Allen *et al.*, "JSC MARS-1: Martian soil simulant," in *Proc. 6th ASCE Specialty Conf. Expo. Eng. Constr. Oper. Space (Space'98)*, Albuquerque, NM, USA, 1998, pp. 469–476.

[16] C. Allen *et al.*, "Martian regolith simulant JSC MARS-1," in *Proc. Lunar Planet. Inst. Sci. Conf. Abstr.*, 1998, vol. 29, p. 1690.

[17] A. Maturili, J. Helbert, T. Roush, and M. D'Amore, "Influence of moisture content on albedo changes of JSC Mars-1 Martian simulant: A lesson for HiRISE?" in *Proc. Lunar Planet. Inst. Sci. Conf. Abstr.*, 2012, vol. 43, p. 1406.

[18] A. Pommerol *et al.*, "Photometric properties of Mars soils analogs," *J. Geophys. Res. Planets*, vol. 118, pp. 2045–2072, 2013.

[19] M. Humayun, "A uniquer piece of Mars," *Science*, vol. 339, pp. 771–772, 2013.

[20] E. Hand, "NASA planners gear up for Martian sample return," *Science*, vol. 334, no. 6186, pp. 787–788, 2014.

[21] B. Kimmel and G. Baranoski, "A novel approach for simulating light interaction with particulate materials: Application to the modeling of sand spectral properties," *Opt. Exp.*, vol. 15, no. 15, pp. 9755–9777, 2007.

[22] G. Baranoski, B. K. T. Chen, E. Miranda, and D. Yim, "Effects of sand grain shape on the spectral signature of sandy landscapes in the visible domain," in *Proc. IEEE Int. Geosci. Remote Sens. Symp. (IGARSS'13)*, Melbourne, Australia, 2013, pp. 3060–3063.

[23] Natural Phenomena Simulation Group (NPSG), *Run SPLITS*, School of Computer Science, Univ. Waterloo, ON, Canada, 2012 [Online]. Available: http://www.npsg.uwaterloo.ca/models/splits.php

[24] G. Baranoski *et al.*, "Rapid dissemination of light transport models on the web," *IEEE Comput. Graphics Appl.*, vol. 32, no. 3, pp. 10–15, May/Jun. 2012.

[25] G. Baranoski, B. K. T. Chen, and E. Miranda, "Simulating the spectral properties of iron-bearing regions of mars using the SPLITS model," in *Proc. IEEE Int. Geosci. Remote Sens. Symp. (IGARSS'14)*, Quebec City, QC, Canada, 2014, pp. 3014–3016.

[26] J. Mustard and J. F. Bell III, "New composite reflectance spectra of Mars from 0.4 to 3.14μm ," *Geophys. Res. Lett.*, vol. 21, no. 5, pp. 353–356, 1994.

[27] J. F. Bell III *et al.*, "Pancam multispectral imaging results from the Spirit rover at Gusev crater," *Science*, vol. 305, pp. 800–806, 2004.

[28] B. C. Clark III *et al.*, "The Viking X ray experiment: Analytical methods an early results," *J. Geophys. Res.*, vol. 82, no. 28, pp. 4577–4594, 1977.

[29] J. Kok, E. Parteli, T. Michaels, and D. Karam, "The physics of wind-blown sand and dust," *Rep. Prog. Phys.*, vol. 75, pp. 1–72, 2012.

[30] A. Mottana, R. Crespi, and G. Liborio, *Simon and Schuster's Guide to Rocks and Minerals*. New York, NY, USA: Simon and Schuster Inc., 1978.

[31] B. Ehlmann, J. Mustard, R. Clark, G. Swayze, and S. Murchie, "Evidence for low-grade metamorphism, hydrothermal alteration, and diagenesis on Mars from phyllosilicate mineral assemblages," *Clays Clay Miner.*, vol. 59, no. 4, pp. 359–377, 2011.

[32] G. Baranoski, B. K. T. Chen, and E. Miranda, "Influence of sand-grain morphology and iron-oxide distribution patterns on the reflectance of sand-textured soils," *IEEE J. Sel. Topics Appl. Earth Observ. Remote Sens.*, vol. 7, no. 9, pp. 3755–3763, Sep. 2014.

[33] M. Vepraskas and D. Cassel, "Sphericity and roundness of sand in costal plain soils and relationships with soil physical properties," *Soil Sci. Soc. Amer. J.*, vol. 51, no. 5, pp. 1108–1112, 1987.

[34] M. Shirazi, L. Boersma, and J. Hart, "A unifying quantitative analysis of soil texture: Improvement of precision and extension of scale," *Soil Sci. Soc. Amer. J.*, vol. 52, no. 1, pp. 181–190, 1988.

[35] W. Eagan and T. Hilgeman, *Optical Properties of Inhomogeneous Materials*. New York, NY, USA: Academic Press, 1979.

[36] W. Roberts, T. Campbell, and G. Rapp, *Encyclopedia of Minerals*, 2nd ed. London, U.K.: Chapman & Hall, 1990, p. 489.

[37] I. Sokolik and O. Toon, "Incorporation of mineralogical composition into models of the radiative properties of mineral aerosol from UV to IR wavelengths," *J. Geophys. Res.*, vol. 104, no. D8, pp. 9423–9444, 1999.

[38] A. Schlegel, S. Alvarado, and P. Wachter, "Optical properties of magnetite (Fe_3O_4)," *J. Phys. C Solid State Phys.*, vol. 12, pp. 1157–1164, 1979.

[39] R. Morris *et al.*, "Mineralogy, composition, and alteration of Mars Pathfinder rocks and soils: Evidence from multispectral, elemental and magnetic data on terrestrial analogue, SNC meteorite, and Pathfinder samples," *J. Geophys. Res.*, vol. 105, no. E1, pp. 1757–1817, 2000.

[40] J. Mustard *et al.*, "The surface Sayrtis Major: Composition of the volcanic substrate and mixing with altered dust and soil," *J. Geophys. Res.*, vol. 98, no. E2, pp. 3387–3400, 1993.

[41] J. F. Bell III, T. McCord, and P. Owensby, "Observational evidence of crystalline iron oxides on Mars," *J. Geophys. Res.*, vol. 95, no. B9, pp. 14 447–14 461, 1990.

[42] A. Krishnaswamy, G. Baranoski, and J. G. Rokne, "Improving the reliability/cost ratio of goniophotometric measurements," *J. Graphics Tools*, vol. 9, no. 3, pp. 31–51, 2004.
[43] B. Kimmel and G. Baranoski, "A compact framework to efficiently represent the reflectance of sand samples," *IEEE Trans. Geosci. Remote Sens.*, vol. 47, no. 11, pp. 3625–3629, Nov. 2009.
[44] G. Baranoski, J. Rokne, and G. Xu, "Virtual spectrophotometric measurements for biologically and physically-based rendering," *Visual Comput.*, vol. 17, no. 8, pp. 506–518, 2001.
[45] B. Kimmel and G. Baranoski, "Simulating the appearance of sandy landscapes," *Comput. Graphics*, vol. 34, no. 4, pp. 441–448, 2010.
[46] R. Morris, D. Golden, J. F. Bell, III, H. Lauer, Jr., and J. Adams, "Pigmenting agents in Martian soils: Inferences from spectral, Mössbauer, and magnetic properties of nanophase and other iron oxides in Hawaiian palagonitic soil PN-9," *Geochim. Cosmochim. Acta*, vol. 57, pp. 4797–4609, 1993.
[47] J. F. Bell III *et al.*, "Mars exploration rover Athena panoramic camera (pancam) investigation," *J. Geophys. Res.*, vol. 108, no. E12, pp. 4-1–4-30, 2003.
[48] F. Nicodemus, J. Richmond, J. Hsia, I. Ginsberg, and T. Limperis, "Geometrical considerations and nomenclature for reflectance," in *Physics-Based Vision Principles and Practice: Radiometry*, L. Wolff, S. Shafer, and G. Healey, Eds. Boston, MA, USA: Jones & Bartlett, 1992, pp. 94–145.
[49] D. Judd, "Terms, definitions, and symbols in reflectometry," *J. Opt. Soc. Amer.*, vol. 57, no. 4, pp. 445–452, 2012.
[50] F. Nicodemus, "Reflectance nomenclature and directional reflectance and emissivity," *Appl. Opt.*, vol. 9, no. 6, pp. 1474–1475, 1970.
[51] F. Nicodemus, "Directional reflectance and emissivity of an opaque surface," *Appl. Opt.*, vol. 4, no. 7, pp. 767–773, 1965.
[52] S. Mekhontsev, A. Prokhorov, and L. Hanssen, "Experimental characterization of blackbody radiation sources," in *Radiometric Temperature Measurements II. Applications*, Z. Zhang, B. Tsai, and G. Machin, Eds. Amsterdam, The Netherlands: Elsevier, 2010, pp. 57–136.
[53] D. Hamby, "A review of techniques for parameter sensitivity analysis of environmental models," *Environ. Monit. Assess.*, vol. 32, pp. 135–154, 1994.
[54] D. Hamby, "A comparison of sensitivity analysis techniques," *Health Phys.*, vol. 68, pp. 195–204, 1995.
[55] F. Hoffman and R. Gardner, "Evaluation of uncertainties in radiological assessment models," in *Radiological Assessment A Textbook on Environmental Dose Analysis*, J. Till and H. Meyer, Eds. Washington, DC, USA: Division of Systems Integration, Office of Nuclear Reactor Regulation, U.S. Nuclear Regulatory Commision, NRC FIN B0766, 1983, ch. 11, pp. 1–55.
[56] X. Ceamanos, S. Douté, J. Fernando, P. Pinet, and A. Lyapustin, "Surface reflectance of Mars observed by CRISM/MRO: 1. Multi-angle approach for retrieval of surface reflectance from CRISM observations (MARS-ReCO)," *J. Geophys. Res. Planets*, vol. 118, pp. 514–533, 2013.
[57] J. Fernando *et al.*, "Surface reflectance of Mars observed by CRISM/MRO: 2. Estimation of surface photometric properties in Gusev Crater and Meridiani Planum," *J. Geophys. Res. Planets*, vol. 118, pp. 534–559, 2013.
[58] H. Hauksdóttir *et al.*, "Mars hyperspectral data processing using ICA and Bayesian positive source separation," in *Proc. AIP Conf. Bayesian Inference Maximum Entropy Methods Sci. Eng.*, 2006, vol. 872, pp. 113–122.
[59] B. Luo, X. Ceamanos, S. Douté, and J. Chanussot, "Martian aerosol abundance estimation based on unmixing of hyperspectral imagery," in *Proc. 2nd Workshop Hyperspectral Image Signal Process. Evol. Remote Sens. (WHISPER'10)*, Reykjavic, Iceland, 2010, pp. 1–4.
[60] M. Vincendon, Y. Langevin, F. Poulet, J.-P. Bibring, and B. Gondet, "Recovery of surface reflectance spectra and evaluation of the optical depth of aerosols in the near-IR using a Monte Carlo approach: Application to the OMEGA observations of high-latitude regions of Mars," *J. Geophys. Res. Planets*, vol. 112, no. E8S13, pp. 1–12, 2007.
[61] M. Wolff *et al.*, "Wavelength dependence of dust aerosol single scattering albedo as observed by the Compact Reconnaissance Imaging Spectrometer," *J. Geophys. Res. Planets*, vol. 114, no. E00D04, pp. 1–12, 2009.

Gladimir V. G. Baranoski (SM'07) received the Ph.D. degree in computer science from the University of Calgary, Calgary, AB, Canada, in 1998.

After the conclusion of his doctorate, he was awarded a 2-year Postdoctoral Fellowship from the National Sciences and Research Council of Canada (NSERC), Ottawa, ON, Canada. In 2001, he became a Faculty Member of the David R. Cheriton School of Computer Science, University of Waterloo, Waterloo, ON, Canada. His research interests include the predictive simulation of light interactions with natural materials and the biophysically based rendering of natural phenomena.

Bradley W. Kimmel received the Bachelor's degree in pure mathematics and computer science and the M.Math. degree in computer science from the University of Waterloo, Waterloo, ON, Canada, in 2002 and 2006, respectively. He is currently working toward the Ph.D. degree in computer science at the Natural Phenomena Simulation Group, David R. Cheriton School of Computer Science, University of Waterloo.

His research interests include simulating light interactions with natural environments.

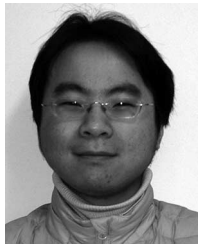

T. Francis Chen received the Bachelor's and Master's degrees in computer science from the University of Waterloo, Waterloo, ON, Canada, in 2006 and 2009. He is currently pursuing the Doctoral degree at the Natural Phenomena Simulation Group, University of Waterloo. His research interests include the predictive simulation of how light interacts with organic and inorganic materials.

Erik Miranda received the B.S.E. and M.Math. degrees in computer science from the University of Waterloo, Waterloo, Canada, in 2010 and 2014, respectively. He is currently pursuing the M.Math. degree in computer science at the Natural Phenomena Simulation Group, David R. Cheriton School of Computer Science, University of Waterloo.

His research interests include the application of computer graphics techniques for acoustic propagation.